Wireless Micropower Instrumentation for Multimodal Acquisition of Electrical and Chemical Neural Activity

Mohsen Mollazadeh, *Student Member, IEEE*, Kartikeya Murari, *Student Member, IEEE*, Gert Cauwenberghs, *Senior Member, IEEE*, and Nitish V. Thakor, *Fellow, IEEE*

***Abstract*—The intricate coupling between electrical and chemical activity in neural pathways of the central nervous system, and the implication of this coupling in neuropathologies, such as Parkinson's disease, motivates simultaneous monitoring of neurochemical and neuropotential signals. However, to date, neurochemical sensing has been lacking in integrated clinical instrumentation as well as in brain-computer interfaces (BCI). Here, we present an integrated system capable of continuous acquisition of data modalities in awake, behaving subjects. It features one channel each of a configurable neuropotential and a neurochemical acquisition system. The electrophysiological channel is comprised of a 40-dB gain, fully differential amplifier with tunable bandwidth from 140 Hz to 8.2 kHz. The amplifier offers input-referred noise below 2 $\mu V_{\rm rms}$ for all bandwidth settings. The neurochemical module features a picoampere sensitivity potentiostat with a dynamic range spanning six decades from picoamperes to microamperes. Both systems have independent on-chip, configurable $\Delta\Sigma$ analog-to-digital converters (ADCs) with programmable digital gain and resolution. The system was also interfaced to a wireless power harvesting and telemetry module capable of powering up the circuits, providing clocks for ADC operation, and telemetering out the data at up to 32 kb/s over 3.5 cm with a bit-error rate of less than 10^{-5}. Characterization and experimental results from the electrophysiological and neurochemical modules as well as the full system are presented.**

***Index Terms*—Brain–computer interface (BCI), biopotential amplifier, chemical sensing, digital telemetry, electrocorticogram (ECOG), electroencephalogram (EEG), inductive coupling, micropower instrumentation, neural interface, neurotransmitters, potentiostat.**

I. Introduction

BRAIN-COMPUTER interfaces (BCI) for neurologic monitoring and neural prostheses rely on sensitive recording of neural activity in the brain which manifests in several signal modalities, including electrical signals such as action potentials (spikes) and local field potentials (LFP) in the brain, and electrocorticogram (ECoG) and electroencephalogram (EEG) signals on the brain surface and scalp [1]. Completely lacking from BCI systems to date is the recording of chemical neural activity, which offers an important neural signal modality for decoding the brain state. These signals are further implicated in several diseases of the central nervous system. If the only purpose of a BCI system is to control a cursor or to move a robotic arm [2]–[4], electrical recordings would suffice. However, a neurochemical monitoring module may advance the future applications of clinical BCI systems, such as closed-loop deep brain stimulation (DBS) for Parkinson's treatment [5].

Electrical and chemical neural activity are tightly coupled in the central nervous system. The presynaptic cells release excitatory or inhibitory neurotransmitters into the synapse upon the arrival of a nerve impulse [6] as illustrated in Fig. 1. These chemical messenger molecules, such as dopamine and glutamate, bind to receptors on the postsynaptic cell and cause excitatory or inhibitory postsynaptic potentials (EPSPs and IPSPs). The neuron integrates all of the postsynaptic potentials and decides whether to fire an action potential or not. The abnormal functioning of this signaling cascade causes severe damage to the underlying cellular substrates. In aging-related neurodegenerative disorders, such as Parkinson's disease, motor functions are disrupted due to the death of dopaminergic neurons in substantia nigra which project to the striatum. This pathway is shown in Fig. 1. In case of cardiac arrest (CA), uncontrolled neurotransmitter release due to the absence of modulatory electrical activity in the brain is the basis of glutamate excitotoxicity which leads to excessive neuronal cell death [7]. Chronic observation of both signals in awake behaving subjects after CA is needed to evaluate the effect of treatments, such as hypothermia [8] on recovery after the brain injury. Other neurotransmitters, such as nitric oxide (NO), are mediators in neurovascular coupling and monitoring their activity can enhance the understanding of cerebrovascular pathology during aging [9].

The interplay between electrical and neurochemical activity is also implicated in several basic neural pathways, such as rewards and learning, and has been neglected in BCI systems. This neurochemical activity contains information about the relationship between presynaptic and postsynaptic activity which, in turn, can modulate LFP activity. The neurochemical activity may also result in the neuronal modulations or rhythms which can be observed in ECoG or EEG recordings. These signal modalities offer a different perspective on neural information for BCI systems. The generation or modulation of these signals

Manuscript received April 14, 2009; revised July 07, 2009. First published November 03, 2009; current version published November 25, 2009. This work was supported in part by NIH/NIA, in part by R01AG029681, in part by NIH MH062444-065296, and in part by the Whitaker Foundation. This paper was recommended by Associate Editor S.-C. Liu.

M. Mollazadeh, K. Murari, and N. Thakor are with the Biomedical Engineering Department, Johns Hopkins University, Baltimore, MD 21205 USA (e-mail: mohsenm@jhu.edu).

G. Cauwenberghs is with the Department of Bioengineering, Jacobs School of Engineering, University of California San Diego, La Jolla, CA 92093 USA (e-mail: gert@ucsd.edu).

Color versions of one or more of the figures in this paper are available online at http://ieeexplore.ieee.org.

Digital Object Identifier 10.1109/TBCAS.2009.2031877

1932-4545/$26.00 © 2009 IEEE

Authorized licensed use limited to: Univ of Calif San Diego. Downloaded on April 20,2010 at 00:53:04 UTC from IEEE Xplore. Restrictions apply.

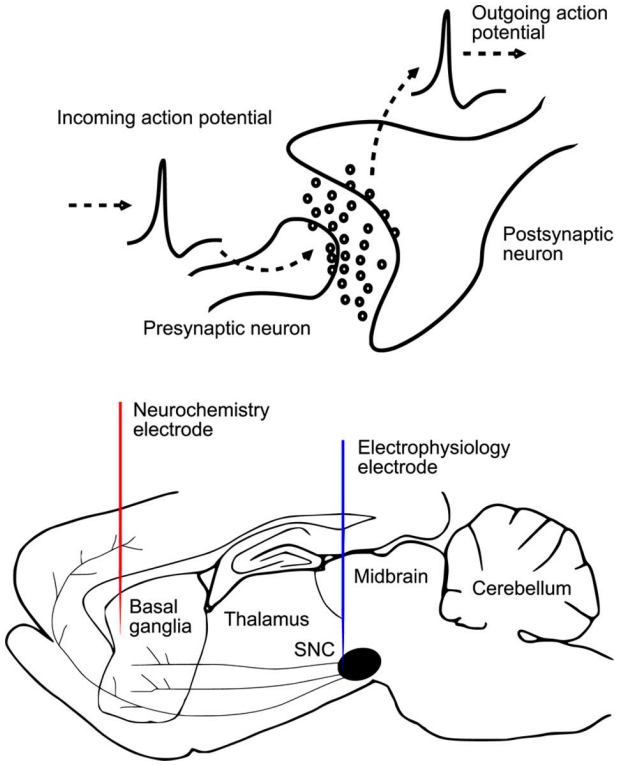

Fig. 1. Neurochemical and neuropotential signaling in the healthy and diseased nervous system. Top: electrical and chemical signaling are intrinsically coupled in synaptic transmission. Bottom: the pathway implicated in Parkinson's disease where dopaminergic neurons in the substantia nigra pars compacta (SNC) degrade. Electrodes show a potential use of simultaneous neurochemical and neuropotential monitoring.

due to neurochemical activity can offer a deeper understanding of brain states which, in turn, can lead to a more stable and accurate BCI system. All of the mentioned applications require low-power simultaneous multimodal acquisition in awake behaving scenarios.

Most of the neural monitoring systems designed to date have focused on one specific signal modality. Several methods have been reported in the literature for monitoring neurotransmitter activity. Some of these are optical and chromatographic methods, positron emission tomography (PET), and single-photon emission computerized tomography (SPECT) [10]–[12]. These methods are mostly indirect, detecting products of reactions involving the neurotransmitter, rather than the neurotransmitter itself and are not amenable to low-power operation in behaving subjects. Alternatively, electrochemical detection of electroactive neurotransmitters [13] can be implemented in very-large-scale integrated (VLSI) systems which offer low power, multiple channels, low noise, and high sensitivity in a very small footprint. Over the years, several groups have presented VLSI potentiostat chips with one or multiple channels. Turner *et al.* [14] used a direct current-to-voltage conversion with an opamp and a resistor with 100-nA sensitivity and a 32-dB dynamic range. In the work presented by Kakerow *et al.* [15], the input current was integrated on a capacitor and the voltage across the capacitor was sampled as a measure of the current leading to an improved sensitivity and dynamic range. Both of these designs were single channel potentiostats. Gore *et al.* described a multichannel semisynchronous $\Delta\Sigma$ analog-to-digital-converter (ADC)-based potentiostat [16] with 50-fA sensitivity and a 60-dB dynamic range. We have previously designed a 16-channel potentiostat with subpicoampere sensitivity and a 140-dB dynamic range using a configurable incremental $\Delta\Sigma$ ADC [17]. Mohseni *et al.* used a programmable second-order $\Delta\Sigma$ modulator along with a wireless interface [18] enabling amperometry as well as cyclic voltammetry.

Recent advances in neuroscience have also driven research in VLSI circuit design for recording electrical activity from the brain. As stated before, these signals can be recorded from within the brain (spike and LFPs), the surface of the brain (ECoG), or from the scalp (EEG). These modalities of neural potentials occupy different frequency bands from 0.1 Hz to 5 kHz and lie in amplitude ranges from 20 to 500 μV [19]. A versatile VLSI system which can interface to all of these modalities is highly desirable. Several VLSI systems have been developed previously [20]–[30] to acquire different neural signals. Typically, the range of frequencies covered by any one of these systems is limited to one or two signal modalities, to accommodate high efficiency for the targeted application.

Recently, Roham *et al.* reported a configurable system for monitoring electrical or chemical activity [31]. Despite acceptable system performance, the VLSI module can work in only one mode at a time. The authors expanded their work by designing a wireless IC for time-shared monitoring of electrical and electrochemical activity [32], [33]. The circuit uses one ADC which is shared between two modalities of the recording. The neurochemical sensing module offers 8.1-pA input current noise in the amperometry mode while consuming 76 μW of power from the supply. The neuroelectrical sensing module has a 5-μV input referred noise while consuming 86 μW of power.

We have previously reported on designing individual modules for monitoring brain activity [34]–[36]. Here, we present an integrated wireless neural interface system for the simultaneous acquisition of neuropotential and neurochemical activity from the brain. The system contains three modules integrated onto two microchips as illustrated in Fig. 2. The neurochemical module consists of a potentiostat with 80-dB dynamic range and picoampere sensitivity for the electrochemical detection of neurotransmitter concentrations down to the nanomolar range. A neuropotential module consists of a 40-dB gain amplifier with a tunable bandpass bandwidth up to 8.2 kHz in order to isolate the signal of interest—spikes, LFPs, ECoG, or EEG. Both neurochemical and neuropotential modules contain incremental $\Delta\Sigma$ ADC which allow programmable digital gain and measurement resolution based on the dynamic range of the acquired signal. A separate microchip integrates a power harvesting and telemetry module [34], which uses electromagnetic induction at 4 MHz to provide power to both microchips. This module also provides ADC clocks, and transmits data from the neurochemical and neuropotential modules at up to 32 kb/s over a distance up to 4 cm with a bit-error rate (BER) less than 10^{-5}. The difference in the spectral content of electrical (hertz to several hundred hertz) and neurochemical signals (megahertz to hertz) is exploited to interleave the digitized bitstreams. Parts of this work have been presented at an invited session in [37]. In this manuscript, we have extensively characterized the effect of wireless data and power transmission on the interface circuitry in terms

Authorized licensed use limited to: Univ of Calif San Diego. Downloaded on April 20,2010 at 00:53:04 UTC from IEEE Xplore. Restrictions apply.

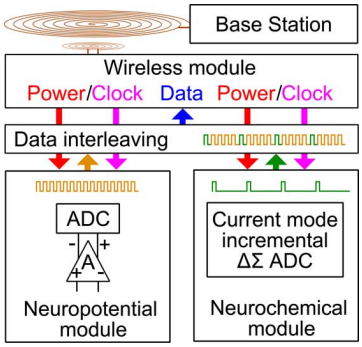

Fig. 2. Functional block diagram of the proposed system. Electrical and chemical activities are monitored simultaneously and the digitized data are transmitted over an inductive link to a base station. The wireless module also provides power and clock for the circuit operation.

of noise performance and compared the theoretical and experimental power transmission efficiencies for the circuit operation. Moreover, simultaneous wireless in-vitro tests performed with the system show stable acquisition of both signal modalities and reveal no significant interference between the neuropotential and neurochemical recordings, and in-vivo tests show EEG signals recorded from the neuropotential module.

II. System Architecture

A. VLSI Potentiostat With Configurable Incremental $\Delta\Sigma$ ADC

The instrumentation required for electrochemical sensing, a potentiostat [35], holds an electrode at a constant potential and measures the resulting current proportional to the analyte concentration. Fig. 3 shows the schematic diagram and operating clocks of the potentiostat circuitry. Nonoverlapping clocks ϕ_1 and ϕ_2 are generated from ϕ^{Δ}. The ratio of periods of ϕ_1 and ϕ^{Δ} sets the oversampling ratio (resolution) of the ADC (four in the example shown in Fig. 3, typically 2^8 to 2^{12}). The rising edge of the clock ϕ_1 starts the conversion by charging the input capacitor C_1 to the redox potential $V_{\rm red}$. Clock ϕ_{1e} occurs within ϕ_1 and resets the integration capacitor C_2 and the comparator capacitor C_3. The integration occurs during ϕ_2 and the integrated value is compared to the midvalue $V_{\rm mid}$. The comparator output is latched by using ϕ^{Δ}. If the latched value D is high, a counter value is incremented and the $\Delta\Sigma$ reference current $i_{{\rm ref}n}$ is subtracted from the input current until the comparator flips. Conversely, when D is low, the counter value does not change and the $\Delta\Sigma$ reference current $i_{{\rm ref}p}$ is added to the input current until the comparator flips. Digital gain in the ADC is implemented by the duty cycle of the clock ϕ^{Δ} (four in the example shown in Fig. 3). The gain is achieved by adding or subtracting the $\Delta\Sigma$ reference currents $i_{{\rm ref}p}$ and $i_{{\rm ref}n}$ to the input current $I_{\rm in}$ only during the high period of ϕ^{Δ}. The gain and OSR can be programmed in the range 1-64 and 2^8-2^{12}. At the end of the integration period, before ϕ_1 goes high, the value in the counter is shifted into a parallel-in serial-out shift register and read out asynchronously.

B. Neuropotential Interface

Fig. 4 shows the block diagram of the neuropotential interface. The bandpass amplifier in the front-end offers fixed-gain (40-dB) amplification with tunable lowpass filtering from 140 Hz to 8.2 kHz. The midband gain is achieved by a fixed capacitance ratio, 100C/C (ratio of input capacitance over feedback capacitance). The dc component of the signal is removed by using the highpass filter implemented using pseudoresistor elements M_{p1} and M_{p2} and capacitor C (100 fF) [22]. Two elements were used in series to increase the resistance and, therefore, decrease the highpass cutoff frequency. The bandpass amplifier was designed by using a two-stage fully differential amplifier with independent common-mode feedback circuitry (CMFB) in each stage. The CMFB is required in the differential structure to stabilize the common-mode level of output voltages [38]. The input transistors (M_1, M_2) were chosen as p-channel devices to lower 1/f noise. They are also sized with large W/L $(216\ \mu/1.8\ \mu)$ to operate in the subthreshold region for the maximum noise-power efficiency. The bias current of the amplifier $(I_{{\rm bias}p})$ is adjusted by using an off-chip programmable digital-to-analog converter (DAC). A decrease in the bias current results in a decrease in the unity gain frequency and, hence, the bandwidth of the amplifier while maintaining the input transistors in the subthreshold region. The amplifier was designed for a maximum unity gain frequency of 800 kHz and a phase margin of 62°. A detailed description of the circuit design can be found in [39].

The amplified neural signal is then digitized by using a configurable incremental $G_m - C$ $\Delta\Sigma$ ADC. In order to digitize the differential output voltage of the amplifier, the amplified signals are first converted to a single-ended current using an nMOS differential pair operational transconductance amplifier (OTA) which also removes any remaining common-mode signal. The OTA input transistors were sized long in order to increase the linear range of operation. The core of the ADC is the same as the structure implemented in the potentiostat circuitry and described in detail in the previous section. This ADC offers programmable resolution from 8 to 12 b and a digital gain of 1 to 4. The digitized output is then read out by using a parallel-in serial-out shift register.

C. Wireless Power Delivery and Telemetry

Fig. 5 illustrates the wireless power delivery and telemetry module coupling inductively and transcutaneously to a base station which supplies power and collects data. The wireless inductive interface is based on a basic principle of electromagnetics—a time-varying current through a coil produces a time-varying magnetic field. Conversely, a time-varying magnetic flux passing through a coil generates an electromotive force (emf) in the coil. Optimal efficiency in power and data transfer depends critically on the geometry of the inductive coupling. We analyzed the effect of coil position and displacement on coupling efficiency between two coils which, in turn, determines the operational range of this module. We present equations governing a simple case with two loops—one being driven by a time-varying current (the primary or transmitter loop) and the other harvesting the resulting magnetic field (the secondary or receiver loop).

We consider a general case where the telemetry or inductive coupling loops may not be coaxial, but have been assumed to be parallel. The mutual inductance between two loops of radii R_P

Authorized licensed use limited to: Univ of Calif San Diego. Downloaded on April 20,2010 at 00:53:04 UTC from IEEE Xplore. Restrictions apply.

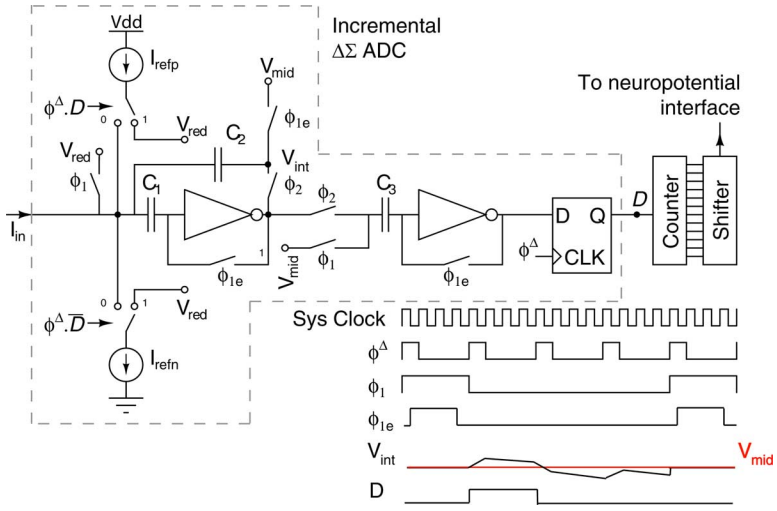

Fig. 3. Schematic block diagram of the VLSI potentiostat circuitry. Clocks on the lower right show an example of operation for gain 4 and oversampling ratio 4.

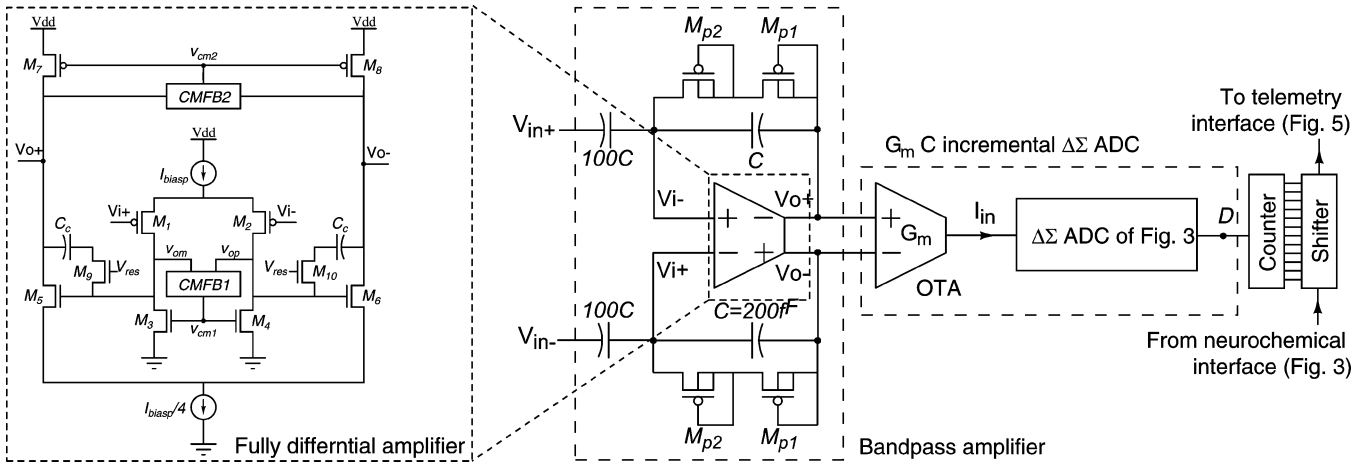

Fig. 4. Functional block diagram for the neuropotential interface channel. The channel consists of a bandpass amplifier and a programmable ADC. A circuit schematic of the fully differential amplifier is shown on the left.

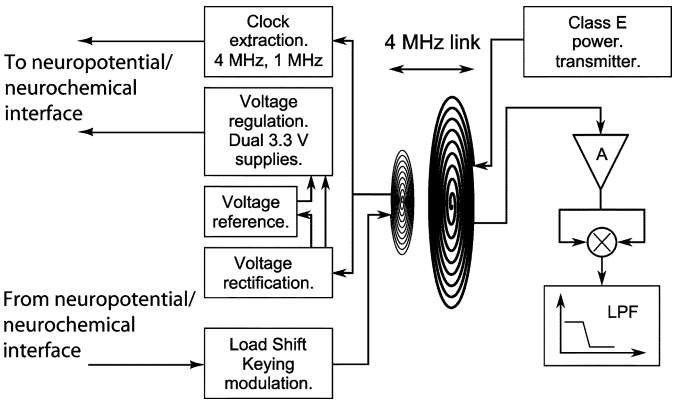

Fig. 5. Functional block diagram for the power harvesting and telemetry block.

and R_S with a planar separation of h and an axial offset of Δ is given by [40]

$$M = \frac{\mu R_P R_S}{2\pi} \oint \frac{\cos\beta}{\sqrt{R_P R_{SL}}} G(r) d\phi \tag{1}$$

with

$$G(r) = \left(\frac{2}{r} - r\right) K(r) - \frac{2}{r} E(r) \tag{2}$$

$$R_{SL} = \sqrt{R_S^2 + \Delta^2 + 2R_S \Delta \cos(\phi)} \tag{3}$$

$$\tan\beta = \frac{\Delta \sin\phi}{R_S + \Delta\cos\phi} \tag{4}$$

$$r = \left(\frac{4R_P R_{SL}}{(R_P + R_{SL})^2 + h^2}\right)^{1/2} \tag{5}$$

where $K()$ and $E()$ are complete elliptic integrals of the first and second kind, respectively, and μ is the permittivity of the medium.

Once the mutual inductance between the two coils is determined, the voltage induced in the receiving coil v_{ind} can be written as [34]

$$v_{\text{ind}} = \frac{\omega M I}{Z} \tag{6}$$

Authorized licensed use limited to: Univ of Calif San Diego. Downloaded on April 20,2010 at 00:53:04 UTC from IEEE Xplore. Restrictions apply.

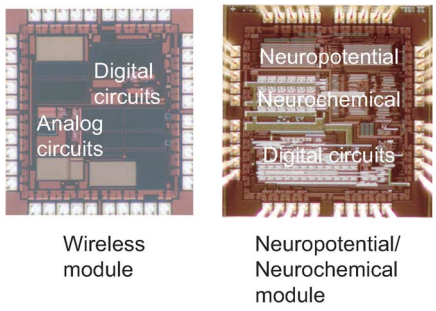

Fig. 6. Mircographs of the fabricated modules in 0.5-μ m CMOS technology. Each die occupies a 1.5-mm × 1.5-mm silicon area.

where Z is a function of the impedance of the secondary coil $(R_s, 1/\omega C_s, \omega L_s)$ and the load R_L being driven by it

$$Z = \left[\left(\frac{\omega L_S}{R_L} + \omega R_s C_s\right)^2 + \left(1 - \omega^2 L_S C_S + \frac{R_S}{R_L}\right)^2\right]^{1/2}. \tag{7}$$

In (6), M is the only geometry-dependent term. Thus, for a given configuration of coils, recalling that power is proportional to the square of the voltage, we can calculate what the theoretical power transfer should be by either numerically calculating or approximating the integral in (1) [40], [41]. Coupling the results from these simulations to the circuit simulations of the wireless module resulted in an operational range of up to 3.5-cm planar separation and 1.1-cm axial offset. The operational range favors the implantable scenario in which the coil positions may not be fixed due to relative movement between the two coils.

While physics describes the relation between the transmitted and received voltages, the induced voltage is a time-varying quantity and needs to be conditioned before it can be used to power a circuit. As illustrated in Fig. 5, the wireless module microchip achieves this by using a rectifier and two independent voltage regulators. The microchip also contains circuits for clock recovery and data modulation using which data can be transmitted on the same link [34]. The base-station transmission coil voltage is driven by a high-efficiency class-E transmitter. On the receiving side, an off-chip coil feeds into a full-wave rectifier, followed by a low-pass filter and two separate regulators, to generate two 3.3-V supplies for the chip operation. Two supplies were used to decouple digital noise from the analog circuits. A clock recovery block extracts a 4-MHz clock that is stepped down to 1 MHz for the ADC operation. The same inductive link can be used for low-rate data transmission. The non-return-to-zero (NRZ) digitized data are transmitted back via load-shift keying (LSK) modulation. It should be noted from (6) and (7) that the load resistance has an effect on the induced voltage. While the voltage regulation should be able to maintain a constant average power level, LSK data transmission may introduce transient noise into the power supplies. This may manifest as variable noise levels at different data-transmission rates.

At the base station, modulation of the load on the secondary coil changes the current flowing through the primary coil. The change in current is converted to a voltage change by using a resistor. The transmitted signal is decoded using coherent demodulation—the voltage is buffered, squared, and lowpass filtered to extract the transmitted data.

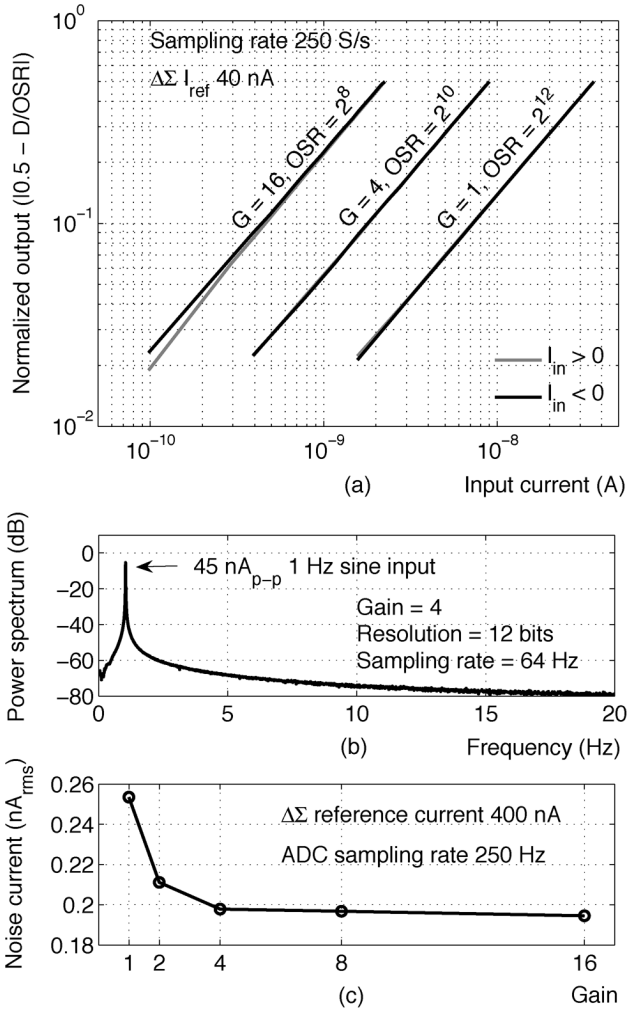

Fig. 7. Characterization results from the potentiostat circuit. a : Normalized digital output of the chip for several values of digital gain G, oversampling ratio OSR, and both polarities of input currents. b is the power spectrum of the output corresponding to 1-Hz 45-nA$_{p-p}$ input current. c is the effect of gain on reducing input current noise.

III. Experimental Results

The combined neurochemical and neuropotential module and the wireless power harvesting and data telemetry module were implemented separately in two 1.5-mm × 1.5-mm microchips in 0.5-μm 3M2P complementary metal–oxide semiconductor (CMOS) technology, fabricated through the MOSIS foundry service. Micrographs of the fabricated chips are shown in Fig. 6. Each module of the system was first characterized independently. For the overall system characterization and for the *in-vivo* recordings, the digital output (or demodulated data) was acquired by using a data-acquistion (DAQ) card (National Instruments, Austin, TX) and read into a computer.

A. Neurochemical Interface

Fig. 7(a) shows the measured normalized digital output of the potentiostat for input currents swept from pA to nA ranges. A

Authorized licensed use limited to: Univ of Calif San Diego. Downloaded on April 20,2010 at 00:53:04 UTC from IEEE Xplore. Restrictions apply.

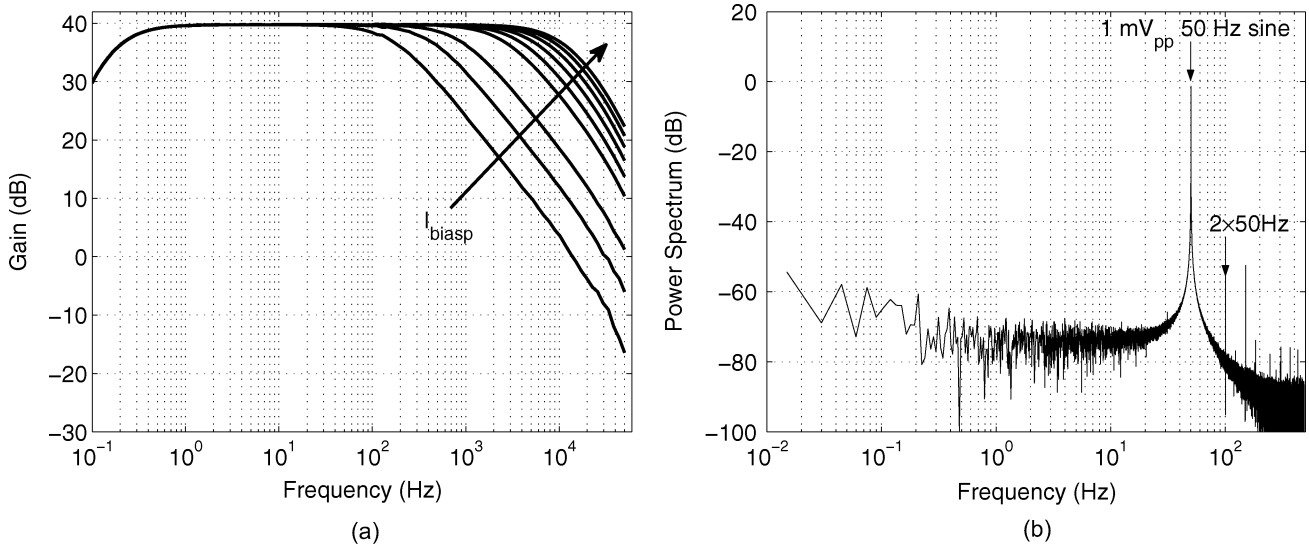

Fig. 8. Neuropotential interface characterization results. a is the amplifier's frequency response for various bandwidths by changing $I_{\mathrm{bias}p}$ from 0.1 to 8 μA and b is the power spectrum of the recorded output when a 1-mV_{p-p} 50-Hz sine wave is presented to the input.

model 6430 sourcemeter (Keithley, Inc., Cleveland, OH) was programmed to vary the input current. The $\Delta\Sigma I_{\mathrm{ref}}$ was set to 40 nA and the system clock was 1 MHz. The digital gain and OSR were programmed individually for each setting for a sampling rate of 250 S/s. As can be seen in the figure, the circuit offers a wide dynamic range for all gain and resolution settings.

Fig. 7(b) shows the power spectrum of the potentiostat output when presented with a 45-nA_{p-p} sinusoidal current at 1 Hz. The $\Delta\Sigma I_{\mathrm{ref}}$ was set to 400 nA. The gain and OSR were set to 4 and 2^{12} respectively, resulting in a sampling rate of 64 S/s. Fig. 7(c) shows the effect of the programmed ADC gain on root mean square (rms) current noise. The OSR was changed for each gain to set the sampling rate to 250 Samples/s. Fig. 7(c) shows the potentiostat input-referred current noise versus the digital gain. The output noise decreases from 1.5 least-significant bit (LSB) for a gain of 1 to 1.1 LSB for a gain of 16 (full scale of 12 b to 8 b, respectively).

B. Neuropotential Interface

The measured gain and bandwidth of the closed-loop bandpass amplifier are shown in Fig. 8(a). The midband gain was 39.6 dB. The amplifier's bandwidth was adjustable from 140 Hz to 8.2 kHz by tuning $I_{\mathrm{bias}p}$ from 0.1 to 8 μA and the low-frequency cutoff was measured to be 0.24 Hz. The amplifier's common-mode rejection ratio (CMRR) and power-supply rejection ratio (PSRR) were larger than 76 dB for inputs between 1 Hz and 10 kHz at an electrode offset of 50 mV. The amplifier total harmonic distortion (THD) was below 1% for inputs within 9.4 mV_{p-p}. For a 250-Hz bandwidth (suitable for EEG recording), the thermal noise level was approximately 100 nV/$\sqrt{\mathrm{Hz}}$. Integration of the PSD from 0.1 Hz to 5 kHz yielded an input-referred noise of 1.65 μV_{rms} and a noise efficiency factor (NEF) [42] of 3.2.

The power spectrum of the digitized output, when a 50-Hz 1-mV_{pp} sine wave was presented to the amplifier, is shown in Fig. 8(b). The amplifier bandwidth was set to 150 Hz. The ADC was set to 10-b resolution and a gain of 1 leading to a sampling rate of 1 kSamples/s. The THD of the channel was measured to be less than 0.3%. The channel noise in terms of LSB was 1.2 LSB (2.5 μV_{rms}), which is suitable for monitoring all modalities of neural potentials.

C. Wireless Power Harvesting and Telemetry

The wireless power harvesting and telemetry module was characterized in two steps. First, only the inductive link was tested by driving the primary coil with a class-E amplifier and monitoring the power delivered to a passive resistive load on the receiving side. Next, the voltage induced in the secondary coil was conditioned by the wireless module circuitry to characterize the voltage regulation and data telemetry and their effect on the input-referred noise of the neural interface.

The primary coil had a diameter of 50 mm and had 10 turns. The secondary coil also had 10 turns, but with a diameter of 20 mm. While a larger secondary coil would harvest power more efficiently, the size is constrained as the coil is meant to be implanted subcutaneously. The frequency of operation was chosen as 4 MHz which has been shown to be optimal for power transfer across biological tissue [43]. Resistive loads of 10 kΩ and 100 kΩ were connected across the secondary coil. The coils were aligned parallel and coaxial, and the distance between them was varied from 10 to 30 mm. Fig. 9(a) shows the ratio of the power received at distance x to the power received at $x = 10$ mm at both loads. The figure also shows the theoretical profile calculated from (6). As can be seen, for both loads, the ratio of the power received as a function of x follows the same trend as the theoretical prediction, although it is consistently lower. This is possibly due to environmental losses not considered in (6). Also, we have assumed that the magnetic field generated by a coil is directly proportional to that generated by a single current carrying loop, which is not the case, given the 3-D geometry of the implemented coils.

Fig. 9(b) shows similar results but for various offset distances between the axes of the coils. Again, the measured values follow the same trends as the predicted values. The reduction is that the induced voltage is less because the magnetic field increases in intensity going from the center to the periphery of the coil. This

Authorized licensed use limited to: Univ of Calif San Diego. Downloaded on April 20,2010 at 00:53:04 UTC from IEEE Xplore. Restrictions apply.

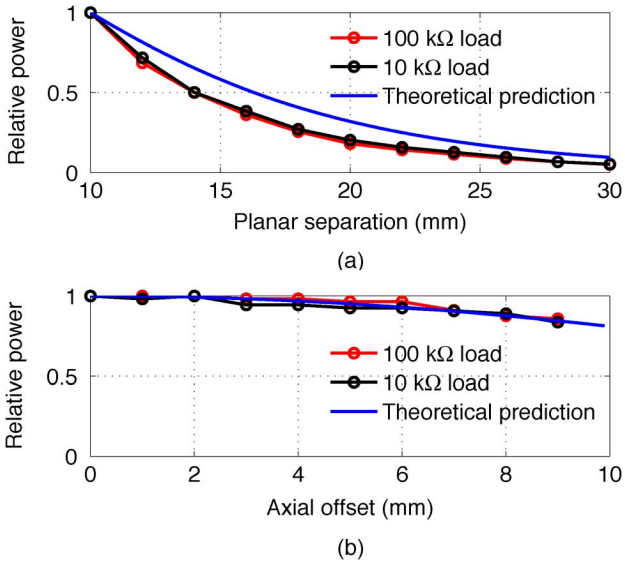

Fig. 9. Fraction of retained power versus displacement (a) parallel and (b) perpendicular to coil axis for two different load conditions as well as theoretical values.

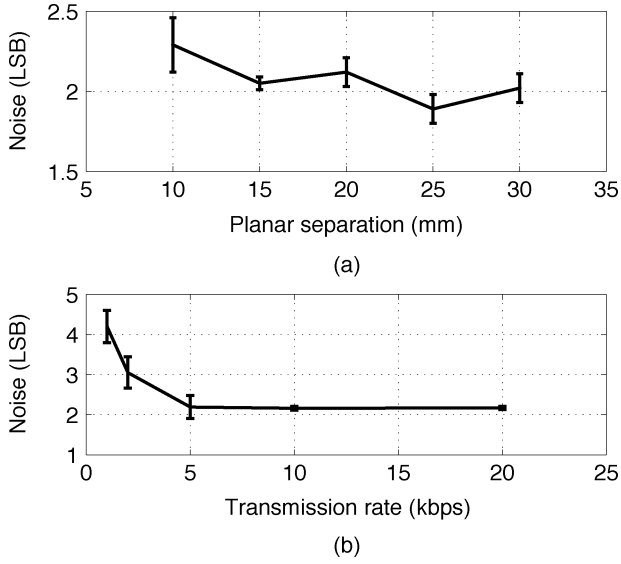

Fig. 11. Measured channel noise versus (a) coil separation and (b) data transmission rate at 25-mm coil separation. Error bars show the standard deviations across five measurements.

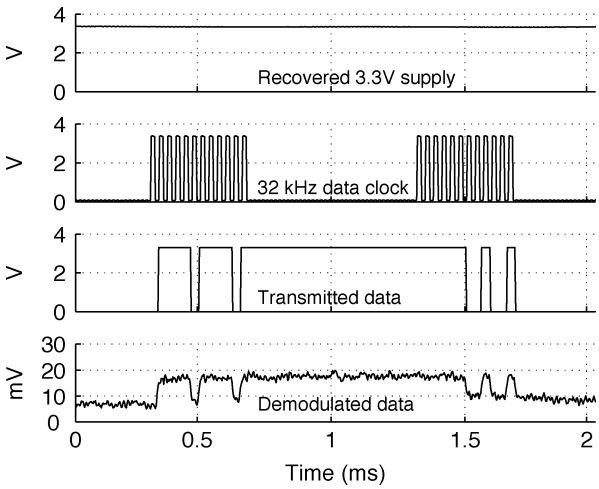

Fig. 10. RF operation: 3.3-V regulated supply, 32-kHz data clock (generated from the 4-MHz recovered clock), transmitted data, and demodulated data at the base station.

makes up for the increased distance between the coils due to the lateral misalignment.

Fig. 10 shows an oscilloscope trace of the regulated 3.3-V supply used to power the neural interface chip (top panel). During the wireless operation of the system, the readout clock (second panel) is generated from the 1-MHz system clock provided by the telemetry module. This clock was used to shift out the digitized neural data (third panel) that modulated a load on the secondary coil. The bottom panel shows the demodulated data at the base station. Stable operation of the circuit was achieved with up to 3.5-cm separation between the coils (less than a 1% change in the regulated voltage supply). Data transmission was also tested up to 32 kb/s, resulting in a bit-error rate (BER) of less than 10^{-5}.

We also characterized the effect of wireless power delivery on noise performance of the neuropotential interface system. Fig. 11(a) shows the measured channel noise for different distances between the coils. As expected, there is more noise in the harvested power supply than the wired power supply leading to an increase in the channel noise from 2 to 2.3 b compared to the maximum noise of 1.1 b in the wired case. The measured channel noise decreased with increasing distance between the two coils, possibly due to reduced electromagnetic interference (EMI) with circuit operation at larger distances and reduced ripple in the regulated supply voltage.

As described before, we used an LSK modulation scheme to transmit the low-data-rate EEG data back to the base station via the same inductive link. This load modulation on the receiver coil results in a modulation of the rectified voltage at the same rate. These fluctuations on the rectified voltage will result in a noise on the regulated supply voltage. The noise on the power supply will, in turn, change the input-referred noise of the system. The relationship between the modulation of received voltage and input-referred noise of the system is highly nonlinear and is not modeled here. Nevertheless, to gain an intuitive understanding of the relationship and to determine the optimal telemetry data rate, we characterized the circuit noise performance for different data-transmission rates.

Fig. 11(b) shows the channel input-referred noise versus the data-transmission rate when the two coils were separated by 25 mm. The rms value of the regulated voltage was 3.27 V. The noise increased rapidly for data rates of less than 5 kb/s. This is likely due to the nature of our modulation scheme, LSK, which operates by changing the load resistance driven by a secondary coil. Assuming a repeated "10" data stream (square wave), from (6) and (7), it can be seen that the input going to the voltage regulator will switch between two levels at the frequency of the data stream. The voltage regulator can be thought of as a proportional controller that keeps the regulated voltage equal to a reference. The controller has a time constant τ which defines how fast it can respond to changes in the input. For changes slower than τ, the controller will be able to respond and change the output in relation to the input. This manifests as a change in the power

Authorized licensed use limited to: Univ of Calif San Diego. Downloaded on April 20,2010 at 00:53:04 UTC from IEEE Xplore. Restrictions apply.

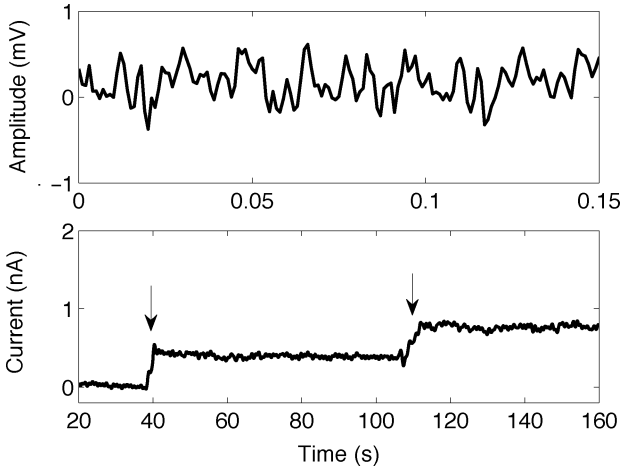

Fig. 12. Recovered EEG data (top panel) and redox current proportional to the dopamine concentration (bottom panel) measured by using the system in an *in-vitro* test in PBS solution. Prerecorded EEG data from rat somatosensory cortex were streamed from a function generator while 1-μM dopamine boluses (arrows) were added to the solution.

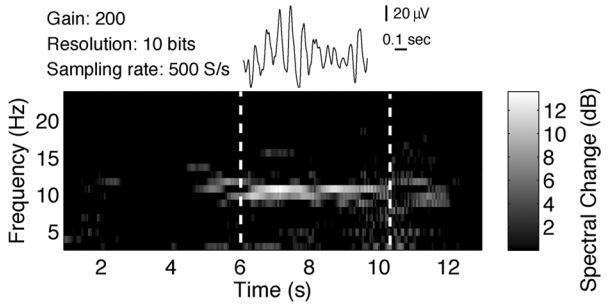

Fig. 13. Time–frequency plot of the recorded EEG waveform from the occipital lobe of a human subject. The dotted line shows closing and opening of the eye. The recorded EEG waveform when the eyes are closed is shown on top. An increase in α band power, which is a feature of eye closure, is visible in the time–frequency plot.

supply that adds more noise to the system. On the other hand, if the input changes faster than τ, the regulator will filter out the high-frequency changes and the output will remain stable.

D. System-Level Characterization

To characterize the overall system-level operation of the combined neural interface and telemetry system, we performed functional tests comprising all three modules simultaneously, and *in-vivo* tests focusing on the neuropotential and telemetry module.

1) Wireless Simultaneous Neurochemical and Neuropotential Recording: Fig. 12 shows the *in-vitro*-acquired data from wireless operation of the system comprising the neurochemical/neuropotential interface chip and the power harvesting and telemetry chip. Prerecorded EEG data from the rat somatosensory cortex were streamed from a function generator to a saline solution while boluses of 1-μM dopamine were added to the solution. Electrochemical detection was performed by using a commercial carbon fiber electrode (CF30-50, WPI, FL) and a Ag/AgCl reference electrode (Bioanalytical Systems, IN). The neuropotential channel was interfaced to the solution by using a screw electrode (PlasticsOne, VA). The neuropotential interface was programmed with a digital gain of 1 and an OSR of 2^{10} leading to a sampling rate of 1 kSamples/s. The neurochemical interface was set to a digital gain of 16 and an OSR of 2^{12}, leading to a sampling rate of 16 Samples/s. The digital output of the chip was recovered after demodulation on the receiver side. The top and bottom panels of Fig. 12 show the recorded EEG and dopamine concentration waveforms, respectively.

2) In-Vivo Wireless EEG Recordings: Although the 8.2-kHz bandwidth of the neuropotential interface by itself is capable of recording spike signals, the telemetry system limits the data transfer to lower bandwidth electrical signals, such as LFPs, since the same link is used for transmitting data as well as power. For BCI applications using EEG or ECoG, the system can support wireless acquisition of these signals. As a proof of concept, EEG recordings were performed on a male human subject fitted with a 20-electrode cap with gel-based electrodes (Electro-Cap, Eaton, OH). A single electrode at position $O1$ was connected to the interface circuit, and the subject was asked to open and close eyes at 4-s intervals. The EEG data were sampled at 500 Hz and digitized to 10 bits. Fig. 13 shows the time–frequency plot of the recorded waveform under wireless operation. The dotted lines denote the closing and opening of the eyes. As can be seen, the power in the 11-Hz band (α activity) increases during eye closure.

IV. Conclusion

We have presented an integrated acquisition system for the wireless recording of neuropotential and neurochemical signals. Multimodal sensing of electrical and chemical activity is provided by a flexible signal acquisition and processing architecture with digitally parameterized frequency corners and midband gains, and with variable decimation parameters in the oversampled data conversion. The presented potentiostat module allows monitoring of electroactive neurochemicals with picoampere sensitivity and offers configurable gain and resolution settings for wide-range sensing. Tunable filters in the neuropotential amplifier front end selectively amplify the signal of interest, ranging from spikes to EEG. The configurable gain and resolution setting in the ADC stage allows the optimum quantization based on the dynamic range and frequency content of the acquired signal. The amplifier's input-referred noise was below 2 $\mu V_{\rm rms}$, consistently providing low-noise performance. The neuropotential and neurochemical interface modules are integrated on a single microchip consuming 140 μW of power from a 3.3-V supply at a sampling rate of 1 kSamples/s.

Electromagnetic induction was modeled over different separations and axial offsets between the coils. Based on the results and the power-conditioning circuitry, we were able to assign an operational range to the power harvesting. The wireless power harvesting module was able to provide the power and clock for interface operation at distances up to 3.5 cm and axial offsets up to 1.1 cm and can transmit data up to a 32-kb/s rate with negligible BER. RF operation increased the input-referred noise of the system from 1.1 to 2.1 LSB. The operation of the complete system comprising neurochemical and neuropotential modules over the wireless link was characterized, and *in-vivo* tests showed acquisition and the wireless transmission of EEG signals. The performance of the system is summarized

Authorized licensed use limited to: Univ of Calif San Diego. Downloaded on April 20,2010 at 00:53:04 UTC from IEEE Xplore. Restrictions apply.

TABLE I
PERFORMANCE SUMMARY OF THE SYSTEM

Neuropotential Interface		
Gain	39.6	dB
Bandwidth	8.2	kHz
ADC Programmable gain	1-4	
Sampling rate	< 16	kS/s
Channel Noise (12 bits)	< 1.1	LSB
Power	< 100	μW
Neurochemical Interface		
Input range	$10^{-12} - 10^{-6}$	A
Channel noise (12 bits)	< 1.5	LSB
ADC Gain	1-64	
Sampling rate	< 1	kS/s
Power	< 42	μW
RF operation		
Harvested supply voltage (dual supplies)	3.27	V
Channel noise (12 bits)	< 2.5	LSB
Bit error rate	$< 10^{-5}$	
Power	35	μW
Operational distance		
planar separation	3.5	cm
coaxial offset	1.1	cm

in Table I. To our knowledge, this is the only system which offers true synchronous monitoring of the neuropotential and neurochemical activity. Moreover, the wireless power transmission makes the system amenable for ambulatory monitoring. However, the low-data-rate telemetry module restrains us from acquiring fast neural signals. Our future work includes designing high-data-rate RF links and simultaneous *in-vivo* monitoring of glutamate concentration and EEG from rat somatosensory cortex following cardiac arrest.

The presented system sets a framework for advancing both clinical aspects of neuroengineering, and research aspects of neuroscience. While typically used neural instrumentation systems are purely electrical or use large and expensive instrumentation for combined neurochemical and neuropotential sensing, the presented integrated system opens a new avenue for the real-time study of the interplay between neurochemical and electrical activity in awake behaving animals. Applications of the system to neuroscience research include studying the cerebrovascular pathology of aging and monitoring of chemical and electrical neural activity in normal and diseased brains. Applications to clinical neuroengineering include future generations of the BCI system, detection of epileptic seizures, and monitoring EEG signals and excitotoxic neurotransmitter activity following global ischemia.

ACKNOWLEDGMENT

The authors would like to thank C. Sauer and M. Stanacevic for the previous design of power harvesting and the telemetry chip and H. Schwerdt and X. Wang for the experiment setup. Chips were fabricated through the MOSIS foundry service.

REFERENCES

[1] G. Dornhege, J. del R. Millan, T. Hinterberger, D. J. McFarland, and K.-R. Muller, *Towards Brain-Computer Interfacing*. Cambridge, MA: MIT Press, 2007.

[2] R. A. Andersen, S. Musallam, and B. Pesaran, "Selecting the signals for a brain machine interface," *Curr. Opn. Neurobiol.*, vol. 14, no. 6, pp. 720–726, 2004.

[3] J. R. Wolpaw, N. Birbaumer, D. J. McFarland, G. Pfurtscheller, and T. M. Vaughan, "Brain-computer interfaces for communication and control," *Clin. Neurophysiol.*, vol. 113, no. 6, pp. 767–791, 2002.

[4] L. R. Hochberg, M. D. Serruya, G. M. Friehs, J. A. Mukand, M. Saleh, A. H. Caplan, A. Branner, D. Chen, R. D. Penn, and J. P. Donoghue, "Neuronal ensemble control of prosthetic devices by a human with tetraplegia," *Nature*, vol. 442, no. 13, pp. 164–171, 2006.

[5] A. Murro, Y. D. Park, G. K. Bergey, E. H. Kossof, E. K. Ritzl, S. C. Karceski, K. Flynn, H. Choi, D. D. Spencer, B. B. Duckrow, and C. Seale, "Multicenter study of acute responsive stimulation in patients with intractable epilepsy," *Epilepsia*, vol. 44, no. S9, pp. 326–, 2003.

[6] M. Bear, B. Connors, and M. Paradiso, *Neuroscience: Exploring the Brain*. Baltimore, MD: Lippincott Williams Wilkins, 2006.

[7] M. Y. Globus, M. D. Ginsberg, and R. Busto, "Excitotoxic index—A biochemical marker of selective vulnerability," *Neurosci. Lett.*, vol. 127, pp. 39–42, Jun. 1991.

[8] R. G. Geocadin, M. A. Koenig, X. Jia, R. D. Stevens, and M. A. Peberdy, "Management of brain injury after resuscitation from cardiac arrest," *Neurologic Clinics*, vol. 26, no. 2, pp. 487–506, 2008.

[9] E. Farkas and P. G. M. Luiten, "Cerebral microvascular pathology in aging and alzheimer's disease," *Prog. Neurobiol.*, vol. 64, no. 6, pp. 575–611, 2001.

[10] R. Braman and S. Hendrix, "Nanogram nitrite and nitrate determination in environmental and biological materials by vanadium (III) reduction with chemiluminescence detection," *Anal. Chem.*, vol. 61, pp. 2715–2718, Dec. 1989.

[11] I. Baranowska and M. Zydron, "Liquid chromatography in the analysis of neurotransmitters and alkaloids," *J. Chromatogr. Sci.*, vol. 40, pp. 224–228, Apr. 2002.

[12] R. Schlosser, "Detection of neurotransmitter interactions with PET and SPECT by pharmacological challenge paradigms," *Nervenarzt*, vol. 71, pp. 9–18, Jan. 2000.

[13] T. Malinski and Z. Taha, "Nitric oxide release from a single cell measured in situ by a porphyrinic-based microsensor," *Nature*, vol. 358, pp. 676–678, Aug. 1992.

[14] R. Turner, D. Harrison, and H. Baltes, "A CMOS potentiostat for amperometric chemical sensors," *IEEE J. Solid-State Circuits*, vol. SSC-22, no. 3, pp. 473–478, Jun. 1987.

[15] R. Kakerow, H. Kappert, E. Spiegel, and Y. Manoli, "Low-power single-chip CMOS potentiostat," in *Proc. 8th Int. Conf. Solid-State Sensors and Actuators and Eurosensors IX. Transducers*, Jun. 1995, vol. 1, pp. 142–145.

[16] A. Gore, S. Chakrabartty, S. Pal, and E. C. Alocilja, "A multichannel femtoampere-sensitivity potentiostat array for biosensing applications," *IEEE Trans. Circuits Syst. I*, vol. 53, no. 11, pp. 2357–2363, Nov. 2006.

[17] M. Stanacevic, K. Murari, A. Rege, G. Cauwenberghs, and N. Thakor, "VLSI potentiostat array with oversampling gain modulation for wide-range neurotransmitter sensing," *IEEE Trans. Biomed. Circuits Syst.*, vol. 1, no. 1, pp. 63–72, Mar. 2007.

[18] M. Roham, D. Daberkow, E. Ramsson, D. Covey, S. Pakdeeronachit, P. Garris, and P. Mohseni, "A wireless IC for wide-range neurochemical monitoring using amperometry and fast-scan cyclic voltammetry," *IEEE Trans. Biomed. Circuits Syst.*, vol. 2, no. 1, pp. 3–9, Mar. 2008.

[19] J. G. Webster, *Medical Instrumentation, Application and Design*. New York: Wiley, 1998.

[20] M. Dorman, M. Prisbe, and J. Meindl, "A monolithic signal processor for a neurophysiological telemetry system," *IEEE J. Solid-State Circuits*, vol. 20, no. 6, pp. 1185–1193, 1985.

[21] R. Martins, S. Selberherr, and F. Vaz, "A CMOS IC for portable EEG acquisition systems," *IEEE Trans. Instrum. Meas.*, vol. 47, no. 5, pp. 1191–1196, Oct. 1998.

[22] R. Harrison and C. Charles, "A low-power low-noise CMOS amplifier for neural recording applications," *IEEE J. Solid-State Circuits*, vol. 38, no. 6, pp. 958–965, 2003.

[23] P. Mohseni and K. Najafi, "A fully integrated neural recording amplifier with dc input stabilization," *IEEE Trans. Biomed. Eng.*, vol. 51, no. 5, pp. 832–837, 2004.

[24] R. Sarpeshkar, W. Wattanapanitch, B. Rapoport, S. Arfin, M. Baker, S. Mandal, M. Fee, S. Musallam, and R. Andersen, "Low-power circuits for brain-machine interfaces," in *Proc. IEEE Int. Symp. Circuits Syst.*, 2007, pp. 2068–2071.

[25] Y. Perelman and R. Ginosar, "An integrated system for multichannel neuronal recording with spike/LFP separation, integrated A/D conversion and threshold detection," *IEEE Trans. Biomed. Eng.*, vol. 54, no. 1, pp. 130–137, Jan. 2007.

Authorized licensed use limited to: Univ of Calif San Diego. Downloaded on April 20,2010 at 00:53:04 UTC from IEEE Xplore. Restrictions apply.

[26] R. R. Harrison, P. T. Watkins, R. J. Kier, R. O. Lovejoy, D. J. Black, B. Greger, and F. Solzbacher, "A low-power integrated circuit for a wireless 100-electrode neural recording system," *IEEE J. Solid-State Circuits*, vol. 42, no. 1, pp. 123–133, Jan. 2007.
[27] J. Aziz, R. Genov, M. Derchansky, B. Bardakjian, and P. Carlen, "256-channel neural recording microsystem with on-chip 3D electrodes," in *Proc. IEEE Tech. Dig. Int. Solid-State Circuits Conf.*, 2007, pp. 160–594.
[28] R. F. Yazicioglu, P. Merken, R. Puers, and C. Van Hoof, "A 60 μW 60 nV/$\sqrt{}$Hz readout front-end for portable biopotential acquisition systems," *IEEE J. Solid-State Circuits*, vol. 42, no. 5, pp. 1100–1110, May 2007.
[29] T. Denison, K. Consoer, W. Santa, A.-T. Avestruz, J. Cooley, and A. Kelly, "A 2 μW 100 nV/$\sqrt{}$Hz chopper-stabilized instrumentation amplifier for chronic measurement of neural field potentials," *IEEE J. Solid-State Circuits*, vol. 42, no. 12, pp. 2934–2945, Dec. 2007.
[30] M. Chae *et al.*, "A 128-channel 6 mW wireless neural recording IC with on-the-fly spike sorting and uwb tansmitter," in *Proc. IEEE Int. Solid-State Circuits Conf. Digest Tech. Papers*, Feb. 2008, pp. 146–603.
[31] M. Roham and P. Mohseni, "A reconfigurable IC for wireless monitoring of chemical or electrical neural activity," in *Proc. IEEE Int. Symp. Circuits and Systems*, May 2008, pp. 1978–1981.
[32] M. Roham, P. A. Garris, and P. Mohseni, "A wireless IC for time-share chemical and electrical neural recording," in *Proc. IEEE Int. Solid-State Circuits Con.—Dig. Tech. Papers*, Feb. 2009, pp. 430–431, 431a.
[33] M. Roham, D. P. Covey, D. P. Daberkow, E. S. Ramsson, C. D. Howard, B. A. Heidenreich, P. A. Garris, and P. Mohseni, "A wireless IC for time-share chemical and electrical neural recording," *IEEE J. Solid-State Circuits*, vol. 44, no. 12, 2009, to be published.
[34] C. Sauer, M. Stanacevic, G. Cauwenberghs, and N. Thakor, "Power harvesting and telemetry in CMOS for implanted devices," *IEEE Trans. Circuits Syst. I, Reg. Papers*, vol. 52, no. 12, pp. 2605–2613, Dec. 2005.
[35] K. Murari, M. Stanacevic, G. Cauwenberghs, and N. Thakor, "Integrated potentiostat for neurotransmitter sensing. A high sensitivity, wide range VLSI design and chip," *IEEE Eng. Med. Biol. Mag.*, vol. 24, no. 6, pp. 23–29, Nov./Dec. 2005.
[36] M. Mollazadeh, K. Murari, H. Schwerdt, X. Wang, N. Thakor, and G. Cauwenberghs, "Wireless multichannel acquisition of neuropotentials," in *Proc. IEEE Biomedical Circuits Systems Conf.*, Nov. 2008, pp. 49–52.
[37] K. Murari, M. Mollazadeh, N. Thakor, and G. Cauwenberghs, "Simultaneous wireless electrophysiological and neurochemical monitoring," vol. 7035, p. 70350Q, 2008, SPIE.
[38] D. J. Johns and K. Martin, *Analog Integrated Circuit Design*. New York: Wiley, 1997.
[39] M. Mollazadeh, K. Murari, G. Cauwenberghs, and N. Thakor, "Micropower CMOS integrated low-noise amplification, filtering, and digitization of multimodal neuropotentials," *IEEE Trans. Biomed. Circuits Syst.*, vol. 3, pp. 1–10, Feb. 2009.
[40] M. Soma, D. Galbraith, and R. White, "Radio-frequency coils in implantable devices: Misalignment analysis and design procedure," *IEEE Trans. Biomed. Eng.*, vol. BME–34, no. 4, pp. 276–282, Apr. 1987.
[41] K. Kim, E. Levi, Z. Zabar, and L. Birenbaum, "Mutual inductance of noncoaxial circular coils with constantcurrent density," *IEEE Trans. Magn.*, vol. 33, no. 5, pt. 3, pp. 4303–4309, 1997.
[42] M. Steyaert and W. Sansen, "A micropower low-noise monolithic instrumentation amplifier for medical purposes," *IEEE J. Solid-State Circuits*, vol. 22, no. SSC-6, pp. 1163–1168, Dec. 1987.
[43] P. Vaillancourt, A. Djemouai, J. Harvey, and M. Sawan, "EM radiation behavior upon biological tissues in a radio-frequency power transfer link for a cortical visual implant," in *Proc. IEEE 19th Annu. Int. Conf. Eng. Med. Biol. Soc.*, Oct./Nov. 2, 1997, vol. 6, pp. 2499–2502, vol. 6.

Mohsen Mollazadeh (S'04) received the B.Sc. degree in electrical engineering from Sharif University of Technology, Tehran, Iran, in 2004 and the M.S. degree in biomedical engineering from Johns Hopkins University, Baltimore, MD, in 2006, where he is currently pursuing the Ph.D. degree.

His research interest includes mixed-signal very-large-scale integrated systems for neural interface, telemetry in implantable systems, and neural mechanism of dexterous hand movements.

Kartikeya Murari (S'02) received the B.Tech. degree in electrical engineering from the Indian Institute of Technology, Madras, India, in 2002, the M.S. degree in biomedical engineering from Johns Hopkins University, Baltimore, MD, in 2004, and is currently pursuing the Ph.D. degree in biomedical engineering at Johns Hopkins School of Medicine.

His research interests lie in mixed-signal very-large-scale integrated design for biomedical applications in sensing, imaging, and power management and in neuromorphic systems.

Gert Cauwenberghs (S'89–M'94–SM'04) received the M.Eng. degree in applied physics from the University of Brussels, Brussels, Belgium, in 1988, and the M.S. and Ph.D. degrees in electrical engineering from the California Institute of Technology, Pasadena, in 1989 and 1994, respectively.

Currently, he is Professor of Bioengineering and Biology at the University of California San Diego, where he co-directs the Institute of Neural Computation. Previously, he was Professor of Electrical and Computer Engineering at Johns Hopkins University, Baltimore MD, and Visiting Professor of Brain and Cognitive Science at the Massachusetts Institute of Technology, Cambridge. His research interests are in advancing silicon adaptive microsystems to understanding biological neural systems, and the development of sensory and neural prostheses and brain-machine interfaces. He pioneered the design and implementation of highly energy efficient, massively parallel microchips that emulate the function and structure of adaptive neural circuits in silicon. His previous contributions include micropower parallel silicon support vector machines for real-time adaptive pattern recognition, and acoustic microarrays for auditory separation and localization.

Dr. Cauwenberghs is a Francqui Fellow of the Belgian American Educational Foundation, and received the National Science Foundation Career Award in 1997, Office of Naval Research Young Investigator Award in 1999, and Presidential Early Career Award for Scientists and Engineers in 2000. He was Distinguished Lecturer of the IEEE Circuits and Systems Society in 2003–2004, and chaired its Analog Signal Processing Technical Committee in 2001–2002. Currently, he is Associate Editor of the IEEE TRANSACTIONS ON BIOMEDICAL CIRCUITS AND SYSTEMS and IEEE TRANSACTIONS ON NEURAL SYSTEMS AND REHABILITATION ENGINEERING. He is a Senior Editor for the *IEEE Sensors Journal*.

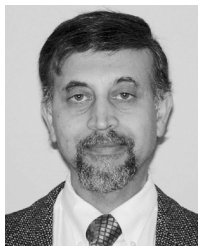

Nitish V. Thakor (S'78–M'81–SM'89–F'97) is a Professor of Biomedical Engineering and Neurology at Johns Hopkins University, Baltimore, MD, where he directs the Laboratory for Neuroengineering. His technical expertise is in the areas of neural diagnostic instrumentation, neural signal processing, optical and magnetic resonance imaging (MRI) of the nervous system, and micro and nanoprobes for neural sensing. He has published 185 refereed journal papers and generated 6 patents and carries out research funded mainly by the National Institute of Health (NIH), National Science Foundation (NSF), and Defense Science Research Council (DARPA). He is the Editor-in-Chief of the IEEE TRANSACTIONS ON NEURAL AND REHABILITATION ENGINEERING and an Associate Editor of several other journals. He is the Director of a Neuroengineering Training program funded by the NIH.

Dr. Thakor is a recipient of a Research Career Development Award from the National Institutes of Health and a Presidential Young Investigator Award from the National Science Foundation, and is a Fellow of the American Institute of Medical and Biological Engineering and Founding Fellow of the Biomedical Engineering Society. He is also a recipient of the Centennial Medal from the University of Wisconsin School of Engineering, Honorary Membership from Alpha Eta Mu Beta Biomedical Engineering student Honor Society.

Authorized licensed use limited to: Univ of Calif San Diego. Downloaded on April 20,2010 at 00:53:04 UTC from IEEE Xplore. Restrictions apply.